Contents lists available at ScienceDirect

Heliyon

journal homepage: www.cell.com/heliyon

Research article

Rapid prototyping of perfusion cell culture devices for three-dimensional imaging of mesenchymal stem cell deposition and proliferation

Taylor E. Scott [a,b], Tim Boccarossa [c], David Florian [a], Melissa A. Fischer [d], Sun H. Peck [b,h], Michael R. Savona [d,e,f,g], Georg Pingen [c], Scott A. Guelcher [a,b,*]

[a] Department of Chemical Engineering, Vanderbilt University, Nashville, TN, USA
[b] Center for Bone Biology, Division of Clinical Pharmacology, Department of Medicine, Vanderbilt University Medical Center, Nashville, TN, USA
[c] Department of Engineering, Union University, Jackson, TN, USA
[d] Division of Hematology and Oncology, Department of Medicine, Vanderbilt University Medical Center, Nashville, TN, USA
[e] Program in Cancer Biology, Vanderbilt University, Nashville, TN, USA
[f] Center for Immunobiology, Vanderbilt University, Nashville, TN, USA
[g] Vanderbilt-Ingram Cancer Center, Vanderbilt University, Nashville, TN, USA
[h] Nashville VA Medical Center, Department of Veterans Affairs, Nashville, TN, USA

ARTICLE INFO

ABSTRACT

Perfusion of porous scaffolds transports cells to the surface to yield cellular constructs for 3D models of disease and for tissue engineering applications. While ceramic scaffolds mimic the structure and composition of trabecular bone, their opacity and tortuous pores limit the penetration of light into the interior. Scaffolds that are both perfusable and amenable to fluorescence microscopy are therefore needed to visualize the spatiotemporal dynamics of cells in the bone microenvironment. In this study, a hybrid injection molding approach was designed to enable rapid prototyping of collector arrays with variable configurations that are amenable to longitudinal imaging of attached human mesenchymal stem cells (hMSCs) using fluorescence microscopy. Cylindrical collectors were arranged in an array that is permeable to perfusion in the *xy*-plane and to light in the z-direction for imaging from below. The effects of the collector radius, number, and spacing on the collection efficiency of perfused hMSCs was simulated using computational fluid dynamics (CFD) and measured experimentally using fluorescence microscopy. The effect of collector diameter on simulated and experimental cell collection efficiencies followed a trend similar to that predicted by interception theory corrected for intermolecular and hydrodynamic forces for the arrays with constant collector spacing. In contrast, arrays designed with constant collector number yielded collection efficiencies that poorly fit the trend with collector radius predicted by interception theory. CFD simulations of collection efficiency agreed with experimental measurements within a factor of two. These findings highlight the utility of CFD simulations and hybrid injection molding for rapid prototyping of collector arrays to optimize the longitudinal imaging of cells without the need for expensive and time-consuming tooling.

---

1. Introduction

The bone marrow microenvironment is responsible for the maintenance of hematopoietic stem and progenitor cell (HSPC) pop-

---

Abbreviations

3DP	3D printing
CAD	Computer-Aided Design
CFD	Computational Fluid Dynamics
CNC	Computer Numerical Control
CV	Coefficient of Variation
ECM	extracellular matrix
EDL	Electrical Double Layer
FFF	Fused Filament Fabrication
hMSC	human mesenchymal stem cells
HSPC	hematopoietic stem and progenitor cell
ISCT	International Society for Cellular Therapy
PS	polystyrene
P_S	Sticking probability
SD	standard deviation
SLA	stereolithography
Stk	Stokes number

---

ulations and incorporates complex cellular, chemical, and structural components necessary to maintain hematopoiesis. The dynamic cell populations and spatial heterogeneity in bone complicate the realization of experimental models of hematopoiesis. While mouse models of bone marrow that are amenable to intravital imaging have been used to visualize cellular interactions, there is a compelling need for 3D *in vitro* humanized models that bridge the gap between traditional 2D cell culture and animal models and also enable visualization of the spatiotemporal dynamics of hematopoiesis. Recently, a 3D perfused bioreactor model of human bone marrow was developed that recapitulates specific aspects of the endosteal niche, including a trabecular bone-like ceramic scaffold, human mesenchymal stem cells (hMSCs), osteoblast-like cells, and extracellular matrix (ECM) secreted by the stromal cells that support the maintenance of HSPCs [1,2]. While the ceramic scaffolds used in these studies mimicked the structure and composition of trabecular bone, their opacity and tortuous pores limited the penetration of light into the interior. Thus, 3D scaffolds that are both perfusable and amenable to fluorescence microscopy are needed to visualize the spatiotemporal dynamics of cells in the bone marrow microenvironment.

Cellular attachment to scaffolds during perfusion is a complex process governed by multiple external forces [3]. The tendency of cells to deviate from the fluid streamlines and intercept the collector is characterized by the Stokes number (*Stk*), which is defined as the ratio between the particle and fluid time scales [4]. Cells suspended in aqueous buffer tend to follow the fluid streamlines (*Stk* « 1) due to the viscous fluid and the small density difference between the cells and water [5], resulting in low collection efficiency [4]. Considering the need to maximize the collection efficiency of high-value hMSCs [4], the effects of collector array geometry and the operating conditions must be better understood to achieve sufficient cell density that promotes cellular proliferation and matrix deposition [6] under the low Stokes flow conditions associated with cell perfusion.

Computational approaches have been applied to investigate the effects of scaffold properties on cellular attachment during perfusion. Computational fluid dynamics (CFD) modeling of scaffolds with triply periodic minimal surface (TPMS) geometries showed that collection efficiency increased with the tortuosity of the pores [7]. Studies combining CFD modeling with particle tracking velocimetry (PTV) experiments found that collection efficiencies and cell densities were low for perfusion of hMSCs through single-fiber poly(ε-caprolactone) meshes fabricated by Fused Filament Fabrication [4,8]. A later study reported that the collection efficiency of single-fiber meshes can be increased by assembling multiple fibers to form multilobed composite scaffolds [9]. While these previous studies provide insight into the design of structures that optimize cell collection efficiency, they enable neither longitudinal imaging of cellular dynamics nor systematic investigation of the effects of array geometry on collection efficiency.

Polystyrene (PS) well plates provide a suitable surface for imaging adherent cells. Due to the difficulties of 3D printing PS, microfluidic PS devices compatible with single-cell imaging have been fabricated by injection molding [10]. However, the expensive and time-consuming process of machining mold tooling limits the utility of this process for rapid prototyping of collector arrays. Previous studies have used stereolithography (SLA) to fabricate molds with high deflection temperatures for injection molding polypropylene [11] and PS [12], which eliminated the need for machining mold tooling.

In this study, a hybrid injection molding approach was designed to enable rapid prototyping of collector arrays with variable configurations that are amenable to longitudinal imaging of adherent hMSCs using fluorescence microscopy. Stationary, support, and ejector pin plates were machined from aluminum using a CNC mill. Prototype collector arrays were created using Computer Aided Design (CAD) and 3D printed (3DP) using stereolithography (SLA). The insert cavity in the support plate was fitted with molds of the

prototype collector array. Cylindrical collectors were arranged in an array that is permeable to light in the z-direction for imaging from below and to fluid flow in the xy-plane to allow perfusion. The effects of the collector radius (a_c), number (N_c), and spacing (S_c) on the collection efficiency of perfused hMSCs was simulated using the particle tracing module in COMSOL and measured experimentally using fluorescence microscopy.

2. Theory and simulation

2.1. Theoretical interception collection efficiency for an array of cylindrical collectors

The capture of small particles dispersed in an aqueous phase is determined by the fluid flow field and by forces that act between the particle and collector, including interception, inertia, diffusion, gravity, electrical double layer (EDL) interactions, attractive London dispersion forces, and repulsive hydrodynamic forces [5]. Diffusion is negligible for micron-sized particles, and the effects of gravity and electrical double layer (EDL) interactions on collection efficiency are described in the **Supplemental Information**.

The Stokes number (Stk) relates the characteristic time of cells (t_c) dispersed in a fluid flow to the characteristic time of the fluid flow field (t_f) [8].

$$Stk = \frac{t_c}{t_f} = \frac{\rho_p a^2 U_0}{9 \mu a_c} \tag{1}$$

where a = cell radius (5 μm), a_c = collector radius (250–500 μm), ρ_p = cell density (1130 kg m^{-3}), μ = fluid viscosity (0.001 Pa s), and U_0 = the superficial fluid velocity far from the obstacle. Inertia dominates the motion of particles dispersed in a gas phase ($Stk > 1$), causing them to detach from the fluid streamlines and intercept the collectors. However, for cells dispersed in water, $Stk \ll 1$ due to the high viscosity of water compared with gases [5] and the small density difference. In the present study, $Stk < 0.0002$, which indicates that the cells follow the streamlines and inertia can be neglected [13]. Suspended cells are assumed to be intercepted by the collector if their center passes within one cell radius of its surface as they follow a grazing streamline (Fig. 1A) [3]. The collection efficiency for
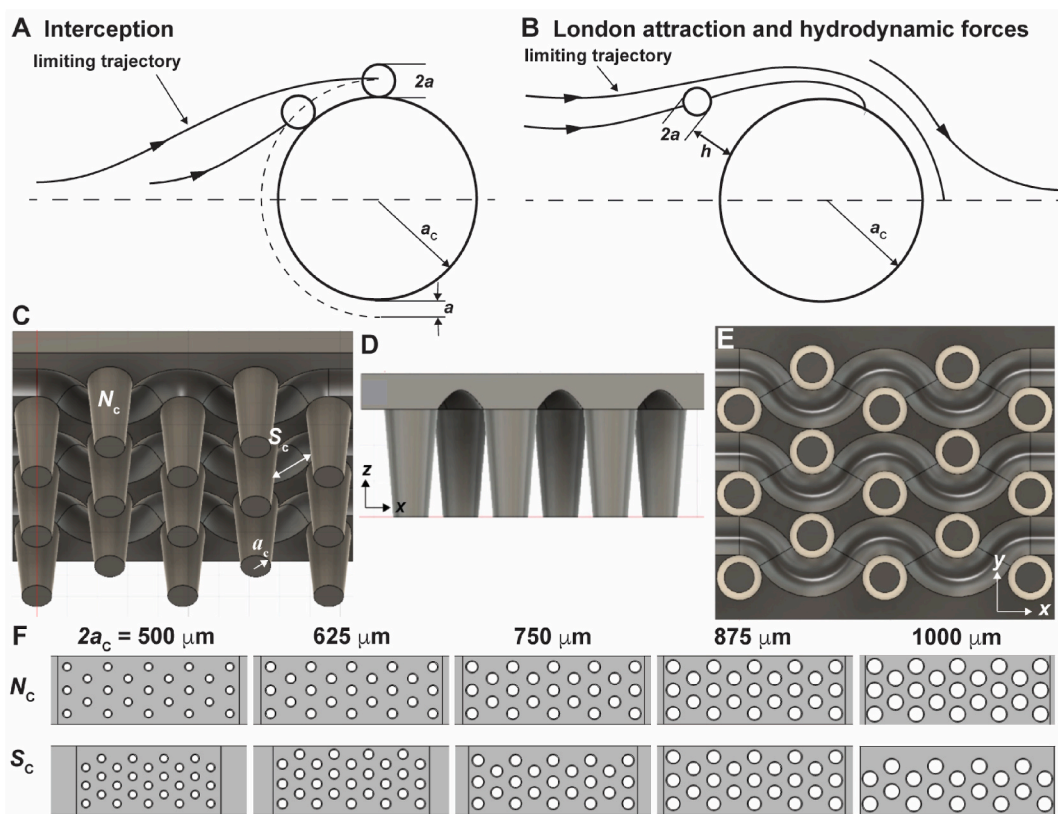
Fig. 1. Design of fluid- and light-permeable cell collector arrays. (A) Schematic depicting the limiting trajectory of an hMSC approaching a cylindrical collector of radius a_c in the absence of external forces. (B) Schematic depicting the limiting trajectory of an hMSC approaching a cylindrical collector of radius a_c in the presence of attractive London dispersion and repulsive hydrodynamic forces. (C–E) CAD renderings of scaffold design: (C) Oblique projection, (D) xz plane showing light-permeable channels aligned with the z-axis, and (E) xy plane detail showing channels permeable to fluid flow. (F) CAD renderings of collector arrays with constant collector number (N_C) or separation (S_C).

interception of cells by an array of cylindrical collectors neglecting external forces is given by: [5]

$$\eta_I = 2A_F \left(\frac{a}{a_c}\right)^2 \tag{2}$$

The structure of the flow is characterized by the parameter A_F, which is a function of the void fraction ϕ for $a/a_c \ll 1$: [13]

$$A_F = \frac{1}{2}\left[-\frac{1}{2}\ln(1-\phi) - \frac{3}{4} + (1-\phi) - \frac{(1-\phi)^2}{4}\right]^{-1} \tag{3}$$

2.2. Dispersion and hydrodynamic forces

As hMSCs approach the collector, attractive London dispersion forces promote cell adhesion while the forced drainage of the viscous liquid from the narrowing gap creates a repulsive hydrodynamic force (Fig. 1B). The adhesion number N_{Ad} is calculated as the ratio of dispersion forces to hydrodynamic forces between the cell and collector:

$$N_{Ad} = \frac{Aa_c^2}{9\pi\mu A_F Ua^4} \tag{4}$$

where A = Hamaker constant = 1.3×10^{-20} J for polystyrene plates interacting across water [3]. For $10^{-6} < N_{Ad} < 10^{-1}$, the theoretical collection efficiency η_t of the array of cylindrical collectors is given by: [13]

$$\eta_t = 2k_1 A_F \left(\frac{a}{a_c}\right)^2 N_{Ad}^{0.059} \tag{5}$$

where k_1 is a constant.

2.3. Collector array design

Truncated cone collectors approximating cylinders were designed to facilitate demolding of the PS collector array. In addition to providing a suitable geometry for testing the validity of interception theory, cylindrical collectors offer the advantages of relative simplicity for theoretical analysis and simulation [5], ease of imaging, and morphological similarity to the rod-like elements in trabecular bone [14]. The collectors were arranged in a pattern such that adjacent columns of cylinders were offset by one collector diameter to design arrays with a tortuosity of 1.15 (Fig. 1D). Five values of collector diameter ($2a_C$) were tested: 500, 625, 750, 875, and 1000 μm (Fig. 1E). The lower end of the range approaches the resolution limits of the injection molding machine [10], while the upper end was selected to maintain at least two collectors in each column of the array. The width, length, and depth of the array were designed as 5, 15, and 1.25 mm, respectively. Collector size was varied under either constant separation (S_c = 650 μm) or constant number (N_c = 23) of collectors. The scaffold was perfused with the hMSC suspension in the xy-plane (Fig. 1D), and cells were imaged from below in the z-direction (Fig. 1C).

2.4. Simulation of hMSC trajectories

The CAD renderings of the light-permeable microfluidic devices were imported into COMSOL to generate a mesh. Due to the small size (a = 5 μm) and low concentration (<0.1 vol%) of the cells, the cellular suspension was modeled as a sparse flow, in which the particles have insufficient inertia to significantly perturb the fluid phase [4,8]. This one-way coupling allows for solving the Navier-Stokes equation (Eq (6)) for the continuous fluid phase first followed by solving the particle motion equation (Eq (7)) [4,7,8].

2.4.1. Governing equations in the continuous phase

The medium was modeled as a continuous, incompressible fluid phase with μ = 0.001 Pa s and ρ = 1000 kg m^{-3}. The Navier-Stokes equations were solved using the COMSOL Multiphysics Computational Fluid Dynamics (CFD) module assuming a fully developed and laminar flow and neglecting external forces (e.g., gravity):

$$\rho\frac{\partial \mathbf{u}}{\partial t} - \mu\nabla^2\mathbf{u} + \rho(\mathbf{u} \bullet \nabla)\mathbf{u} + \nabla p = 0, \nabla \bullet \mathbf{u} = 0 \tag{6}$$

where $\mathbf{u}$ is the fluid velocity and p is pressure [7,8]. The output pressure was selected as zero and a no-slip boundary condition imposed on the walls of the PS collectors.

2.4.2. Governing equations in the dispersed cellular phase

hMSCs were modeled as uniformly distributed discrete spherical particles with radius a = 5 μm. Their motion is modeled using the particle motion equation, which equates the particle inertia with the drag and gravitational forces acting on the particles in a Lagrangian framework: [8,15]

$$\frac{\mathrm{d}u_p}{\mathrm{d}t} = \frac{9\mu}{2\rho_p a_c^2}\frac{C_d Re}{24}(u - u_p) + \frac{g(\rho_p - \rho)}{\rho_p} \tag{7}$$

where u_p = cell velocity, g = gravitational constant (9.81 m s^{-2}), C_d = drag coefficient for spherical particles, and Re=Reynolds number ($\rho u a_c/\mu$) [7,8].

2.4.3. Simulated rate of cell deposition on collectors

The COMSOL Multiphysics Particle Tracing Module was used to simulate the deposition rate of hMSCs dispersed in the fluid phase on the collectors by tracking the particles along the continuous phase streamlines calculated from the Navier-Stokes equation. The mesh design is described in Supplemental Fig. S1. While the flow-field could be modeled accurately on a relatively coarse mesh, the mesh near the collector surface must be refined to smaller than $0.5a$ to accurately track the particles near the collectors. The Particle Counter feature was used to count the number of particles that intercept the surface of the trabecular collectors. 292 cells were released into the 292 µl collector array every 0.5 s for a total of 20 releases. Cells that approached the collectors within $0.5a$ were assumed to have been collected (sticking probability P_S = 100 %, Supplemental Fig. S1D). This method for counting collected cells was chosen due to the design of the Particle Tracing Module, which tracks each cell using the location of its centroid without considering its size. Thus, if a cell centroid is located within $0.5a$ of a collector, that cell was assumed to have deposited on the collector surface.

2.5. Calculation of collection efficiencies

The dimensionless cell removal rate, known as the collection efficiency η, is calculated from the overall particle deposition rate (I) normalized by the convective flux of cells toward the projected area of the collector:

$$\eta = \frac{cell\ deposition\ rate}{convective\ flux\ of\ cells\ toward\ projected\ area\ of\ collector} = \frac{I}{2a_c h_d U C_0} \tag{8}$$

where $2a_c h_d$ = projected area of a cylindrical collector. Eq (8) was modified to account for the fact that in the experiments and simulations, the number of cells deposited on an individual collector ($n_{cells,i}$) at the endpoint were counted. In the experiments, a suspension of hMSCs with concentration $C_0 = 10^6$ cells ml^{-1} was perfused through the collector array at superficial velocity U. The collection efficiency is given by:

$$\eta_{E,i} = \frac{\#\ of\ collected\ cells}{convective\ flux\ of\ cells\ toward\ projected\ area\ of\ collector} = \frac{n_{cells,i}/t_p}{2a_c h_d U C_0} \tag{9}$$

where t_p = perfusion time (s) and h_d = 1.25 mm and w_d = 5 mm are the thickness and width of the collector array, respectively. In the COMSOL simulations, the total number of cells perfused through the array (n_0 = 5840 cells) was specified. Thus, the individual collector efficiency is calculated from the number of cells deposited on a specific collector divided by the total number of cells that flowed toward the projected area of the collector:

$$\eta_{S,i} = \frac{\#\ cells\ on\ collector\ i}{\#\ cells\ that\ flow\ past\ collector\ i} = \frac{n_{cells,i}}{n_{cells,0}\left(\frac{2a_c h_d}{w_d h_d}\right)} = \frac{n_{cells,i}}{n_{cells,0}(2a_c/w_d)} \tag{10}$$

The overall collection efficiency is calculated as the total number of cells deposited on all collectors ($n_{cells,t}$) divided by the total number of cells that flowed toward the projected area of an individual collector and the total number of collectors N_c:

$$\eta_{E,o} = \frac{n_{cells,i}/t_p}{2a_c h_d U C_0 N_c} \tag{11}$$

$$\eta_{S,o} = \frac{n_{cells,t}}{n_{cells,0}(2a_c/w_d)N_c} \tag{12}$$

The overall collection efficiency was calculated from all the collectors for the simulations and for the 5 collectors that were imaged by fluorescence microscopy. Overall experimental and simulated collection efficiencies were fit to Eq (5) to determine k_1 from the η_o versus $2a_c$ data for the constant N_c and S_c array designs.

3. Material and methods

3.1. Materials

Molds were 3D printed by SLA using the Form 3 printer and Hi Temp Resin supplied by Formlabs (Somerville, MA). PS microfluidic devices were injection molded using an APSX-PIM Plastic Injection Machine (APSX). The mold and ejector plate were machined from Tight-Tolerance Multipurpose 6061 Aluminum with Certificate, Precision Ground (McMaster-Carr). Pull-out dowel pins (¼" diameter by ¾" long, McMaster-Carr) were used as ejector pins. PPR-PS01 general purpose PS (GPPS) pellets with a Melt Flow Index (MFI) of 11

at 200 °C under a 5-kg load were supplied by Premier Plastic Resins (Lake Orion, MI). PS microfluidic devices were tissue-culture treated using a PlasmaFlo PDC-FMG plasma cleaner (Harrick Plasma). The cell culture chamber was creating by attaching the PS devices to glass microscope slides (24 × 60 mm, Chemglass Life Sciences) and inlet/outlet ports (Leur Lock Chip Connection Ports w/ wide base, Darwin Microfluidics) using a UV-curable adhesive (Ultra Light-Weld 3025, Dymax). Channels were coated with collagen from calf skin (Sigma-Aldrich) and fibronectin (Corning).

3.2. Cells

Human mesenchymal stem cells from bone marrow (hMSC) were purchased from PromoCell (catalog number C-12974). hMSCs were tested by the vendor using a number of assays, including morphology; proliferation potential; adherence; viability; flow cytometric analysis of a comprehensive panel of markers recommended by the ISCT [16]; adipogenic, osteogenic, and chrondrogenic markers; HIV-1, HIV-2, HBV, HCV, HTLV-1, and HTLV-2 assays; and microbial contaminants (fungi, bacteria, and mycoplasma). Cells were labeled with CellTracker CM-Dil Dye (553/570 nm, Invitrogen) and grown in growth medium consisting of Mesenchymal Stem Cell Growth Medium 2 (PromoCell) supplemented with SupplementMix (PromoCell) and 1 % Penicillin-Streptomycin (10,000 U/mL, Gibco). PBS (1X) without calcium and magnesium and 0.05 % Trypsin,0.53 mM EDTA (1X) were also used for cell culture (Corning). A LIVE/DEAD Viability/Cytotoxicity Kit (ThermoFisher Scientific) and CellTiter 96 Aqueous Non-Radioactive Cell Proliferation (MTS) (Promega) were used to assess cell viability and proliferation, respectively.

3.3. Fabrication of PS microfluidic devices

PS collector arrays were injection molded using an APSX-PIM 5-ton/345-bar injection molding machine (Fig. 2A). The mold in the APSX-PIM machine (Fig. 2B) consists of an aluminum stationary plate (Fig. 2C) and an aluminum support plate (Fig. 2D). The mold cavity in the support plate includes an inset (Fig. 2E), which is 3D printed using SLA from the array designs shown in Fig. 1F. An ejector plate (Supplemental Fig. S2) with pins to demold the PS collector array from the support plate (Fig. 2D) was designed in Fusion 360 and machined from aluminum. The injection-molded PS collector array (Fig. 2F) was mounted on an inverted microscope stage for fluorescence microscopy (Fig. 2G). Each of the components of the mold is described in detail below.

3.3.1. Machining of aluminum stationary and support plates

Surface runners and gates were machined into the stationary and support halves of the mold (Fig. 2C) using a PM-833 TV Ultra Precision Milling Machine (Precision Matthews, Coraopolis, PA) converted to CNC. Surface runners and gates were sized to decrease shear stresses during filling to reduce poor surface cosmetics [17]. The gate depth was selected as 53 % of the wall thickness of the part (4.7 mm) based on the MFI of PS and the thin-walled design of the collector array [18]. The gate width was calculated from the following equation:
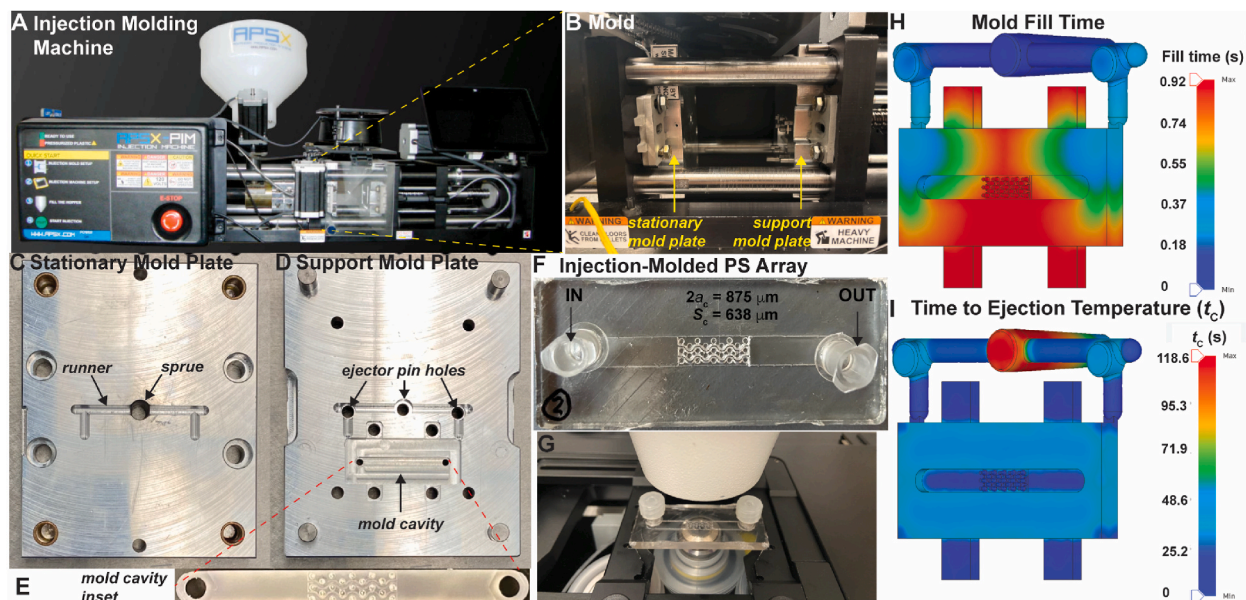
Fig. 2. Manufacture of PS collector arrays. (A) Injection molding machine. (B) Stationary and moving mold plates. (C) Aluminum stationary mold plate with the sprue and runners. (D) Aluminum support mold plate showing the ejector pin holes, mold cavity, and 3D-printed mold cavity insert for the PS array. (E) SLA-printed mold of the PS collector array. (F–G) Photos of the (F) injection-molded PS collector array (G) installed on the fluorescent microscope stage. (H–I) Fusion 360 injection molding simulations of the (H) mold fill time and (I) time to ejection temperature.

$$W = n \times \left(\sqrt{A} \right) \div 30 \tag{13}$$

where n is a material constant (n = 0.6 for PS) and A is the surface area of the cavity (in^2). The runners were chosen as full round runners to provide the least amount of shear. The last runner branch feeding into the gate is 1.5 times the wall thickness and the feed runner diameter was calculated as follows:

$$D_{feed} = D_{branch} \times N^{\frac{1}{3}} \tag{14}$$

where N = 2 is the number of runner branches [18].

Ejection pin holes were drilled in the support mold plate (Fig. 2D) to facilitate removal of the rigid PS collector array using an ejector plate (Supplemental Figure S2). The mold fill time and time to ejection temperature were simulated from the CAD model and Fusion 360 injection molding simulations (Fig. 2H and I). The simulations were performed for a representative PS resin (GPPS Styron 678 D (AmSty), MFI = 10), a melt temperature of 200 °C, and mold surface temperature of 25 °C. Simulation conditions were adjusted to ensure proper filling of the mold and optimize the barrel and mold temperatures and the hold and cooling times on the injection molding machine.

3.3.2. 3D printing of the scaffold mold by stereolithography (SLA)

Molds were designed in Autodesk Fusion 360 and converted to an STL file. PreForm was used as the slicing software, with adaptive layer thickness ranging from 28 to 100 μm, default print settings, and full raft supports. Molds were printed at 35 °C using a Formlabs Form 3 SLA printer with laser spot size = 85 μm and xy resolution = 25 μm from High Temp Resin, which has a heat deflection temperature (HDT) of 238 °C at 0.45 MPa. Printed molds were washed with isopropanol for 15 min and cured under UV light for 30 min.

3.3.3. Injection molding of PS microfluidic devices

Collector arrays were injection molded from the SLA-printed inserts using GPPS pellets at the conditions listed in Table 1. To prepare devices for cell culture, the devices were milled on a Bantam Tools Desktop CNC Milling Machine using surface facing to ensure a smooth, even surface for attaching a glass microscope slide. A 1/8", 2 flute flat end mill was used with a feed rate of 1000 mm min^{-1}, plunge rate of 127 mm min^{-1}, and spindle speed of 6000 min^{-1} at a facing depth of 0.15 mm. Inlet and outlet holes were drilled with a 1.3-mm drill bit (McMaster-Carr), and the devices were sonicated in 70 % ethanol for 30 min. To prepare the PS devices for cell culture, the arrays were O$_2$ plasma treated for 3 min, and glass microscope slides (24 × 60 mm) and inlet and outlet ports were attached using a UV curable adhesive (Ultra Light-Weld 3025, Dymax) to prepare the devices for perfusion and imaging. To sterilize the devices, the channels were soaked in 70 % ethanol for 1 h followed by three 30-min PBS washes. To promote cell attachment, the channels were coated with a collagen type 1 solution (6 μg/cm^2, calf skin, Sigma-Aldrich) for 3 h at 37 °C, followed by three 10-min PBS washes. Arrays were then coated with a fibronectin solution (5 μg/mL, Corning) overnight at 4 °C followed by two 10-min PBS washes before cell seeding.

3.4. CFD simulations

COMSOL Multiphysics and the CFD and Particle Tracing Modules were used to simulate streamlines, shear stress distributions, and cell deposition on the collector arrays. A stationary study with laminar flow physics was used to simulate the flow of fluid (modeled as water) through the collector array at an initial fluid velocity of 9.79 mm s^{-1} assuming a no-slip boundary condition at the wall and a zero-pressure outlet condition. Velocity field plots with 100 points were generated to show the fluid streamlines through the collector arrays, and a shear stress contour plot was created to show the shear stress distributions.

A time-dependent study with particle tracing was added to the laminar flow physics study to simulate particle flow through the collector array. Cells were modeled as 10-μm diameter spherical particles with density = 1130 kg m^{-3}. The sticking probability (P$_S$) at the wall was assumed to be 1. The drag force and gravity force were included in the force balance. 292 particles were released every 0.5 s for 10 s, and particle counters were used to count the collected particles on the cylindrical collectors.

3.5. Perfusion of microfluidic devices with hMSCs

3.5.1. Cell culture and labeling

hMSCs were plated at 4000 cells cm^{-3} in growth medium. Cells were cultured in a humidified 37 °C/5 % C O$_2$ incubator, allowed to

Table 1
Injection molding parameters for the 5-ton AZPX-PIM V2 plastic injection molding machine with piston diameter 1 cm, maximum injection volume 30 cm^3, and 1250 W heating power.

	Barrel T, °C	Mold T, °C	Injection P, bar	Hold P, bar	Clamping F, tons	Hold t, s	Cooling t, s	Clamp t, s
Max.	315	315	345	345	5	N/A	N/A	N/A
Exp.	200	20	215	140	3.5	8.5	38	10.6

grow to confluence, and labeled with CellTracker CM-Dil Dye (553/570 nm).

3.5.2. Calibration curve

A calibration curve was prepared to correlate fluorescence intensity with the number of hMSCs. 25,000, 50,000, 100,000, 300,000, 500,000, and 1,000,000 cells were seeded in each well of a six-well plate in 2 mL growth medium and allowed to attach for 3 h. Fluorescence intensity was measured using a Zeiss LSM 710 META inverted confocal microscope, plotted versus cell number (Supplemental Fig. S3), and fit to a linear least-squares model to yield the relationship $I = 2726 n_c$, where n_c is the number of cells.

3.5.3. Perfusion of hMSCs

After labeling, hMSCs were collected by trypsinization then seeded directly in the perfusion bioreactor in growth medium at 10^6 cells/mL at a superficial velocity of 10, 33, or 56 mm s^{-1} for 6 h. The perfusion bioreactor consisted of the microfluidic device hooked up to a peristaltic pump (Masterflex Ismatec Reglo Digital Multichannel Pump) to perfuse cells and media through the channel. Media was recirculated through the flow loop and the flow direction reversed every 5 min for the first h of seeding then every hour for the next 5 h. For proliferation experiments, the cells were cultured for a week and culture medium was changed every 2–3 days.

3.5.4. Fluorescent imaging

Confocal microscopy was performed on a Zeiss LSM 710 META Inverted microscope equipped with long UV (405 nm), blue/green (458, 488, 514 nm), green/red (561 nm), and red/far-red (633 nm) lasers. All scans were acquired at 37 °C and 5 % CO$_2$ in the bidirectional mode with z-spacing of 7.94 μm. Images were acquired with a 10x/0.50 Fluar objective and 0.6x optical zoom at 1024 × 1024 resolution. CM-Dil imaging was done using the 514 nm laser/AlexaFluor 555 channel. Live/dead imaging was done using the 488 nm laser/FITC channel for live cell staining and the 514 nm laser/AlexaFluor 532 channel for dead cell staining.

3.5.5. Assessment of cell viability

To assess cell viability, a LIVE/DEAD Viability/Cytotoxicity Kit was used. Cells were cultured in the Sc-875 device as described above for 6 h. 5 μL calcein AM and 20 μL ethidium homodimer-1 were added to 10 mL PBS. The staining solution was added to the channel of the device and incubated for 30 min at 25 °C. After imaging, cells were collected by trypsinization for 5 min at 37 °C. Cells
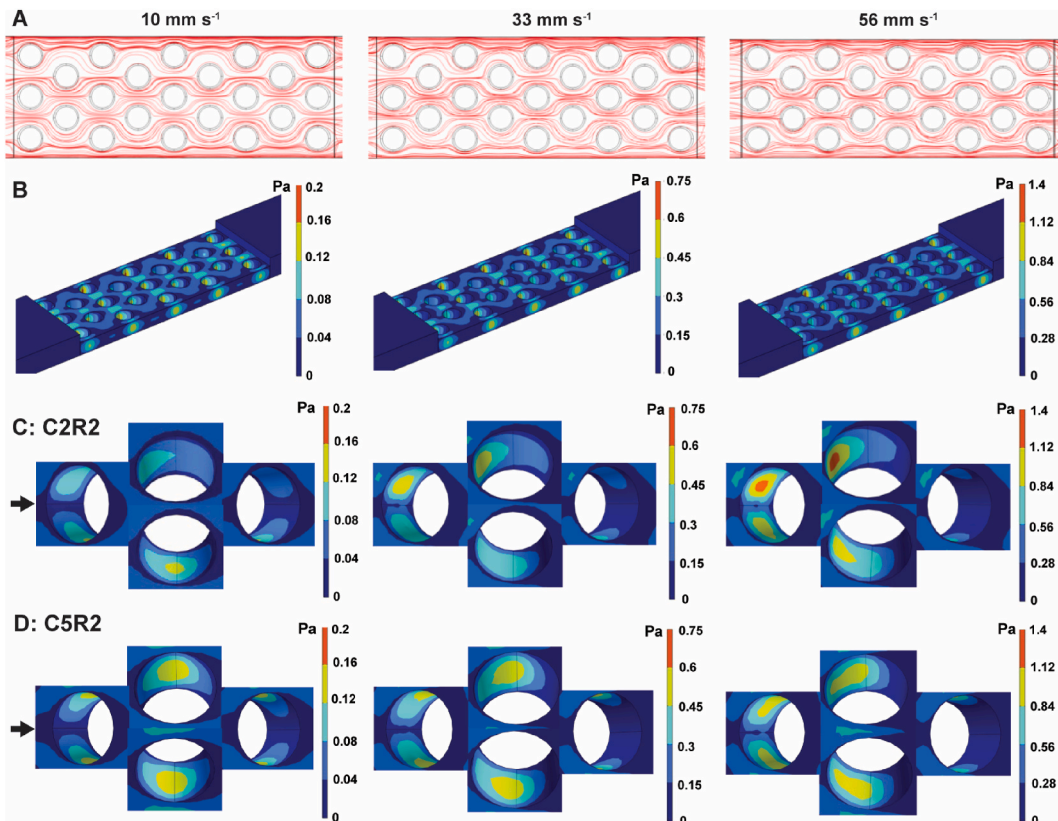
Fig. 3. CFD simulations for the Sc-875 collector array. (A) Fluid streamlines and (B) shear stress distributions at superficial velocities $U_0 = 10$, 33, and 56 mm s^{-1}. (C–D) Shear stress distributions near the (C) C2R2 and (D) C5R2 collectors at superficial velocities $U_0 = 10$, 33, and 56 mm s^{-1}. Arrows indicate the direction of flow.

were centrifuged and resuspended in 500 μL of growth medium. 10 μL cells and 10 μL trypan blue were added to a cell counting slide (Bio-Rad) and cell counts and viability were assessed using a Bio-Rad TC10 Automated Cell Counter.

3.5.6. Assessment of cell proliferation

To assess cell proliferation, hMSCs were labeled with CellTracker CM-Dil dye and seeded in the perfusion bioreactor as described above. Cells were cultured for a week and devices were imaged by confocal microscopy on days 1, 4, and 7. Culture medium was changed every 2–3 days. CellTiter 96 Aqueous Non-Radioactive Cell Proliferation Assay (MTS) was also used to assess proliferation. On days 1, 4, and 7, 20 μL of the MTS solution and 100 μL of culture medium were injected into the channel of the device and incubated for 1 h at 37 °C/5 % CO_2. Absorbance was read at 490 nm using a plate reader.

4. Results

4.1. Design and fabrication of PS microfluidic devices amenable to fluorescence microscopy

Injection-molded PS collector arrays (Fig. 2E) were manufactured for the constant N_c and constant S_c designs (Fig. 1F) using a hybrid injection molding approach, which enabled rapid prototyping of nine distinct collector array designs (the Sc-875 array, which is the base case design, is identical to the Nc-875 array). Mold cavity inserts for the arrays were 3D printed using SLA, thereby limiting the machined tooling to the aluminum stationary, support, and ejector plates. The effects of collector radius a_c for the constant N_c and constant S_c array designs on hMSC collection efficiency were investigated using fluorescence microscopy.

4.2. CFD simulations of fluid streamlines and shear stress distributions

The fluid streamlines for the Sc-875 array at superficial velocities $U_0 = 10, 33,$ and 56 mm s^{-1} are shown in Fig. 3A. The streamlines and shear stress distributions for all arrays ($U_0 = 10 \text{ mm s}^{-1}$) are shown in Supplemental Figs. S4 and S5, respectively. The upper end of the range of superficial velocities was previously reported for seeding hMSCs in porous scaffolds in a perfusion bioreactor [1]. The fluid flows around the collectors, creating shear stresses near the surface (Fig. 3B). The maximum values of τ_w are 0.2, 0.75, and 1.3 Pa for $U_0 = 10, 33,$ and 56 mm s^{-1}. Higher magnification images of the shear stress distributions near the C2R2 and C5R2 collectors are shown in Fig. 3C and D. The shear stress was highest at an angle from the horizontal of about 45° as the fluid approached the cylindrical surface and decreased as the fluid flowed past the trailing surface.
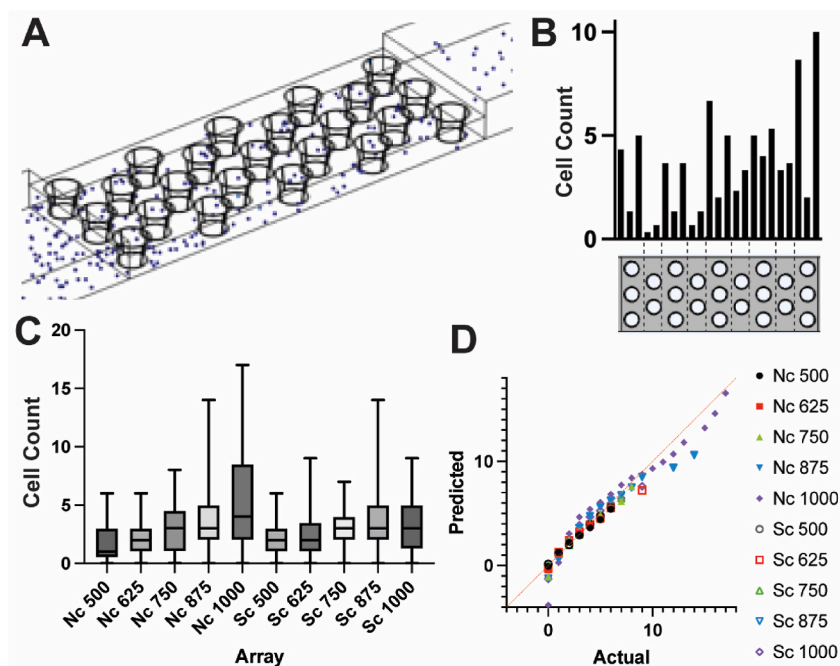
Fig. 4. Simulation of cell collection using the Particle Tracing Module in COMSOL. (A) Image of cells attached to the collectors or domain boundaries at the end of the simulation for the Sc-875 array. (B) Histogram of collected cell counts for the 875-μm array (average of 3 runs). (C) Frequency distribution of cells attached to all collectors in each array. (D) Q-Q plot showing the normality of the distribution of cells attached to all collectors in each array.

4.3. CFD simulations of hMSC collection

hMSC trajectories and attachment to the collectors were simulated using the Particle Tracing module including gravitational and hydrodynamic forces in COMSOL. Cells within $0.5a_C$ from the collector were assumed to attach with a sticking probability $P_S = 1$ (Supplemental Fig. S1D). A representative simulation of attached cells after flow through the Sc-875 array shows cells attached to the collectors (Fig. 4A). Cells that settled on the lower surface of the array due to gravity were also observed. A representative histogram of cells attached to each collector in the Sc-875 array is shown in Fig. 4B (average of 3 runs). Images of collected cells and histograms for the other arrays are shown in Supplemental Fig. S6. The frequency distribution of collected cells on each array is shown in Fig. 4C. The mean, standard deviation (SD), and coefficient of variation (CV) are listed in Table 2. The CV ranges from 50 to 90 %, which indicates a relatively high degree of variability in cell counts on each array. While the log-normal distribution more accurately models the collision efficiency data for cell suspensions flowing through porous media [19,20], some of the cylinders collected zero cells, which cannot be fit to a log-normal distribution. The D'Agostino & Pearson test was applied to the cell counts simulated for all the collectors in each array over the three independent replicates to determine if they were normally distributed (Table 2) [21]. Cell count distributions that pass the test are not inconsistent with a Gaussian distribution, while those that fail the test ($p < 0.05$) are not sampled from a Gaussian distribution. Q-Q plots reveal the deviation from normality for several of the distributions (Fig. 4D). Frequency distributions for all collector arrays are skewed toward higher values, as evidenced by the positive skewness (γ_1, Table 2). The majority of distributions exhibit positive kurtosis (γ_2, Table 2), which indicates that there are more values in the tails compared with the Gaussian distribution.

4.4. Optimal cell seeding conditions and kinetics of hMSC collection

Due to the low Stokes number, hMSCs tend to follow the fluid streamlines, and thus only cells in grazing streamlines have the potential to attach to the collector (Fig. 1A). Therefore, multiple passes are needed to achieve sufficient cell density for hMSC expansion and osteogenic differentiation, but cell death increases with shear stress and the number of passes. To identify the perfusion conditions that optimize collection of viable hMSCs, the Sc-875 array was perfused for 6 h at $10 \leq U_0 \leq 56$ mm s^{-1}. Representative images of live (green)/dead (red) staining show more live cells at the lowest velocity (Fig. 5A). The overall fluorescence intensity for all 5 collectors showed the highest number and percentage of live cells at $U_0 = 10$ mm s^{-1}, and the number of live cells decreased with increasing U_0 (Fig. 5B). Similar results were observed from the cell count data, which showed the highest hMSC viability (88 %) at $U_0 = 10$ mm s^{-1} (Fig. 5C). Thus, hMSC seeding was performed at superficial velocity $U_0 = 10$ mm s^{-1} in all future experiments. The kinetics of cell collection was measured longitudinally using fluorescence microscopy at 1.5, 3, 4.5, and 6 h. Representative z-stack images of collectors C2R2 and C5R2 show increasing fluorescence with seeding time (Fig. 5D). The average cell counts calculated from the fluorescence calibration curve (Supplemental Fig. S3) show that the number of collected cells increased with seeding time (Fig. 5E). The overall fluorescence intensity (averaged over the 5 collectors that were imaged) as a function of collector diameter and array type at 6 h (Fig. 5F) was used to calculate the cell counts (Fig. 5G). With the exception of the 1000-μm collector, the cell counts were higher for the constant S_c arrays than the constant N_c arrays.

4.5. Individual collection efficiencies

The individual collection efficiencies calculated from the experimental and simulated cell counts for collectors C2R1, C2R2, C5R2, C7R2, and C8R2 using Eq (5) are shown in Supplemental Figure 7 for the constant S_c and N_c arrays. The average experimental and simulated individual collection efficiencies ranged from 0.0001 to 0.006 and were within the same order of magnitude.

4.6. Overall collection efficiencies

The frequency distribution of cells on each of the 5 collectors is shown for each array in Fig. 6A. The mean, standard deviation (SD), and coefficient of variation (CV) are listed in Table 3. The CV ranges from 50 to 146 %, which is greater than that observed for the simulations (Table 3) and is larger for the constant N_c (105 %–157 %) compared with the constant S_c (69.9 %–83.5 %) arrays. The D'Agostino & Pearson test was applied to the cell counts simulated for all the collectors in each array over the three independent

Table 2
Descriptive statistics for the simulated frequency distributions for each collector array. CV = coefficient of variation, SD = standard deviation, γ_1 = skewness, and γ_2 = excess kurtosis. The p value from the D'Agostino & Pearson test determines whether the data pass or fail the normality test.

	Constant N_c					Constant S_c				
$2a_c$,μm	500	625	750	875	1000	500	625	750	875	1000
Mean	1.70	2.29	2.96	3.64	5.41	2.11	2.28	2.86	3.64	3.44
SD	1.52	1.58	2.12	2.85	4.56	1.56	1.98	1.48	2.85	2.72
COV	89.5 %	69.1 %	71.8 %	78.3 %	84.2 %	73.8 %	86.5 %	51.8 %	78.3 %	79.1 %
γ_1	0.823	0.674	0.694	1.31	0.865	0.299	0.898	0.173	1.31	0.918
γ_2	0.008	−0.201	−0.386	2.12	−0.304	−0.482	0.464	0.083	2.12	−0.135
p	0.0258	0.0743	0.0541	<0.0001	0.0175	0.313	0.0049	0.775	<0.0001	0.0402
Pass?	No	Yes	Yes	No	No	Yes	No	Yes	No	No
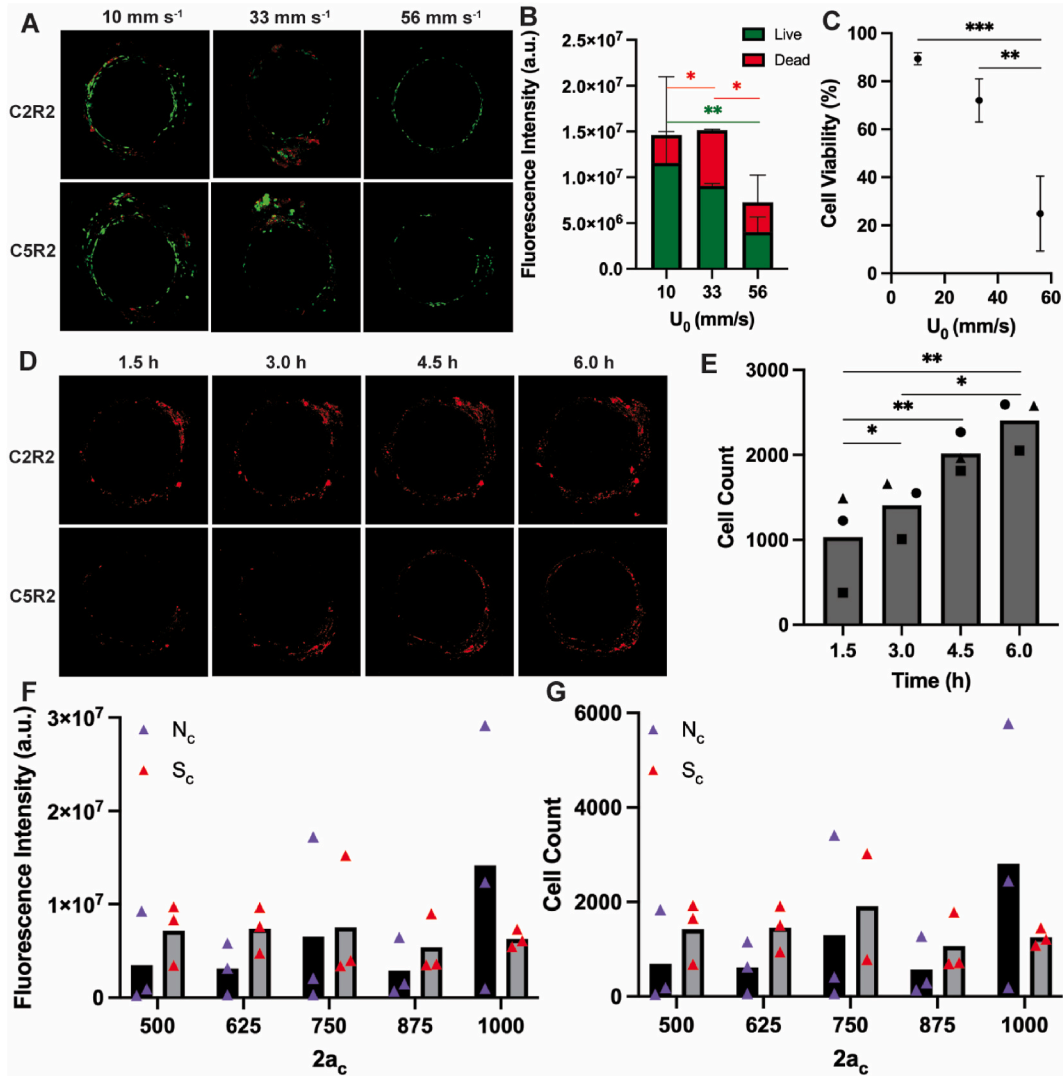
Fig. 5. Optimal cell seeding conditions and kinetics of hMSC collection. (A) Representative z-stack images of live/dead staining of cells at 10–56 mm s^{-1} and 6 h. (B–C) Viability of hMSCs calculated from (B) live/dead staining and (C) cell counts as a function of superficial velocity U_0. (D) Representative z-stack images of the S_c-875 C2R2 and C2R5 collectors at 1.5, 3, 4.5, and 6 h at $U_0 = 16$ mm s^{-1}. (E) Counts of hMSCs versus time at $U_0 = 10$ mm s^{-1}. (F–G) Average (F) fluorescence intensity and (G) cell counts as a function of collector diameter for the constant N_c and S_c arrays at $U_0 = 16$ mm s^{-1} and 6 h n = 3, *p < 0.05., **p < 0.01, ***p < 0.005.

replicates to determine if they fit a normal or log-normal distribution (Table 3) [21]. The inverse likelihood ratio ($\frac{1}{LR} = \frac{P_{\log-normal}}{P_{normal}}$, where P = probability) exceeded unity for all arrays, indicating that the data are more likely represented by a log-normal distribution. All but two of the distributions passed the test, which indicates that they are not inconsistent with a log-normal distribution (p < 0.05). Q-Q plots show good agreement between actual cell counts and those predicted from the log-normal distribution (Fig. 6B). The overall collection efficiencies were calculated from the simulated and experimental cell counts for collectors C2R1, C2R2, C5R2, C7R2, and C8R2 using Eq (11) for the constant N_c (Fig. 6C) and constant S_c (Fig. 6D) arrays. The simulated overall collection efficiencies exceed the experimental values for all arrays, but the agreement is within a factor of two for the constant S_c arrays (Fig. 6D). Experimental and simulated overall collection efficiencies were fit to the dispersion and hydrodynamic forces model (Eq (5)) using k_1 as a fitting parameter (Fig. 6E and F). The interception model, which neglects the effects of external forces, over-predicts collection efficiency, suggesting that repulsive hydrodynamic forces exceed the attractive dispersion forces. For the constant N_c arrays, the simulated and experimental collection efficiencies followed a trend opposite that predicted by the hydrodynamic model (Eq (5), Fig. 6E), indicating a poor fit ($R^2 < 0$). However, for the constant S_c arrays, the hydrodynamic model follows the trend of collector diameter with collection efficiency for both the simulated and experimental trajectories (Fig. 6F). Values of k_1 calculated from the nonlinear regression of simulated and experimental trajectories are listed in Table 4. These findings suggest that the correlation for the shape factor A_F (Eq (3)) may be a poor predictor of spatial effects for the constant N_c arrays [3].
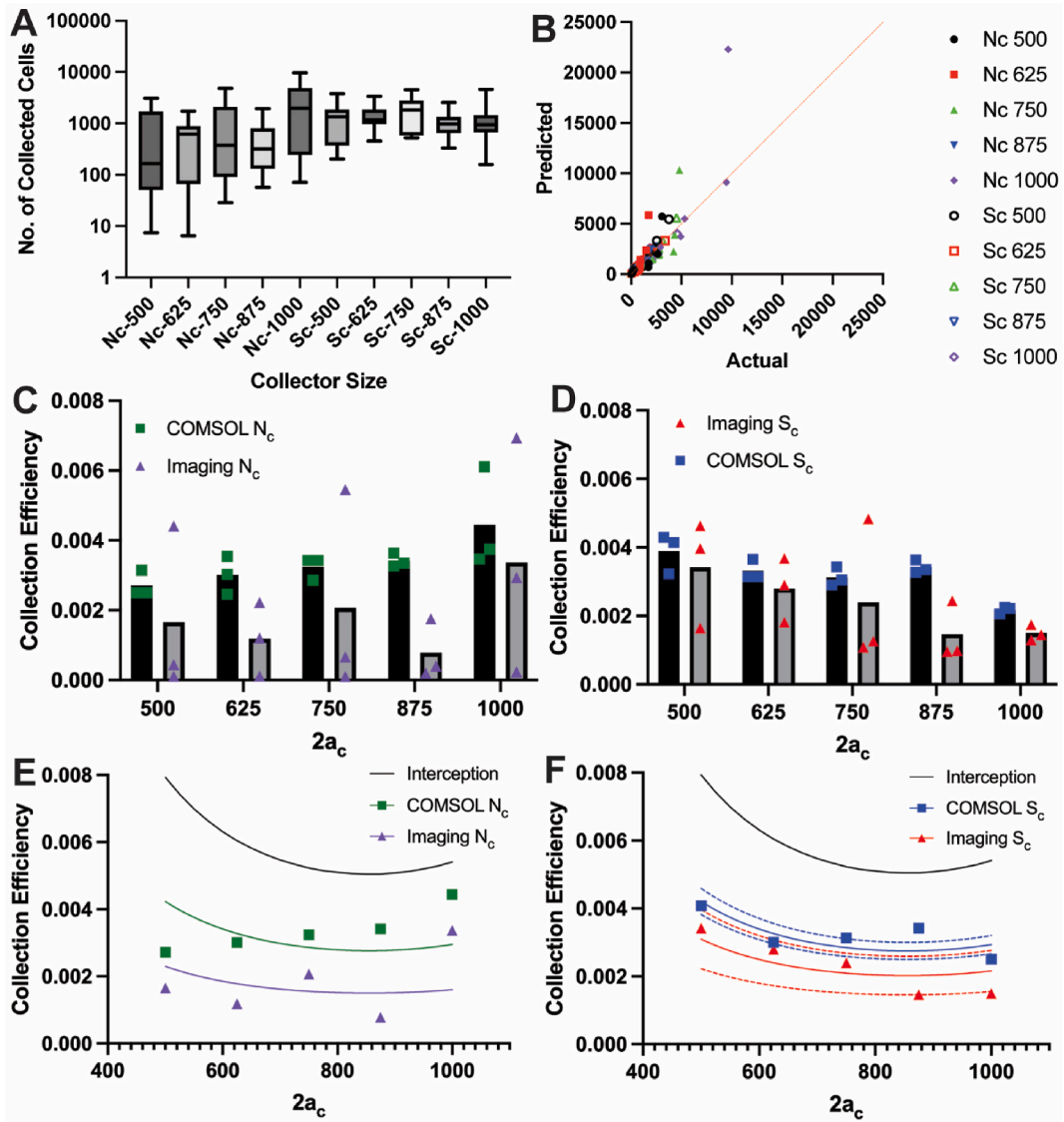
Fig. 6. Overall collection efficiencies. (A) Overall frequency distribution of collected cells on the 5 imaged collectors for each array. (B) Q-Q plot comparing actual collected cell counts with those predicted by the Gaussian distribution. (C–D) Comparison of overall collection efficiencies calculated from the COMSOL simulations and fluorescence imaging experiments for the (C) constant N_c and (D) constant S_c arrays. (E–F) Comparison of collection efficiencies calculated from interception theory and fits to the vdW-H theory. Dashed lines represent 95 % CI.

Table 3
Descriptive statistics for the experimental frequency distributions for each collector array COV denotes coefficient of variance, SD denotes standard deviation.

	Constant N_c					Constant S_c				
$2a_c$, μm	500	625	750	875	1000	500	625	750	875	1000
Mean	738.9	614.7	1296	572.0	2808	1422	1458	1905	1066	1248
SD	1076	534.9	1742	598.7	3210	995	740	1355	643	1042
CV	146 %	87.0 %	134 %	105 %	114 %	69.9 %	50.8 %	71.1 %	60.3 %	83.5 %
Skew	1.38	0.714	1.30	1.38	1.32	0.761	1.13	0.634	1.23	2.57
Kurt	0.445	−0.056	0.112	0.830	0.845	0.669	1.82	−0.368	1.072	8.26
LR^{-1}	3.4×10^6	4.6	6.6×10^5	1.4×10^3	3.8×10^3	2.2	4.8	3.7	15.7	145
p	0.068	0.443	0.088	0.048	0.057	0.297	0.050	0.630	0.066	<0.0001
Pass?	Yes	Yes	Yes	No	Yes	Yes	Yes	Yes	Yes	No

Table 4
Values of k_1 determined from the nonlinear regression of collection efficiencies for constant S_c arrays. CI = Confidence Interval.

| Parameter	Simulated	Experimental
Best fit	94.95	69.87
Lower 95 % CI	86.24	50.25
Upper 95 % CI	103.7	89.48
R^2	0.2869	0.2026

4.7. Proliferation of collected hMSCs

To determine whether attached hMSCs expand to form a confluent monolayer on the collector surface, hMSCs were cultured in growth medium on the Sc-875 array for 7 days. Collectors C2R1, C2R2, C5R2, C7R2, and C8R2 were imaged by fluorescence microscopy longitudinally on days 1, 4, and 7. Representative images for C2R2 and C5R2 show increasing fluorescence with time, which is not uniformly distributed near the surface of the collector (Fig. 7A). While there was significant variation between collectors, the cell counts on each individual collector as well as the average for the five collectors imaged increased monotonically with time (Fig. 7B). The overall cell proliferation for all collectors assessed by MTS assay shows an increase in absorbance from day 1–7 (Fig. 7C). The fluorescence and MTS data indicate that cells proliferated on the collectors for up to 7 days.

5. Discussion

In this study, the effects of cylinder diameter and array geometry on the collection efficiency of hMSCs was assessed by fluorescence microscopy and CFD simulations. Collector arrays that were amenable to perfusion and imaging of attached hMSCs were fabricated by hybrid injection molding, which enabled rapid prototyping of cylindrical collector arrays with variable geometric configurations. Shear stresses <0.2 Pa resulted in collection of cells with high viability that proliferated over 7 days to form a dense layer of cells on the surface. Experimental collection efficiencies agreed within a factor of 2 with simulated values and followed a trend with cylinder diameter similar to that predicted by collision theory for arrays with constant separation between collectors. The separation between collectors was 650 μm for the constant S_c arrays and ranged from 513 to 1013 μm for the constant N_c arrays, which is within the range for trabecular bone (700–1000 μm [22,23]). Correlations for the geometry factor A_F are generally poor [3] but more accurately predicted the effects of cylinder size on collection efficiency for the constant S_c arrays compared with the constant N_c arrays.

Trabecular bone has been modeled as a mixture of cylindrical rods and plates, with the relative ratios of each component a function of anatomic site, disease state, and age [24]. Bone-templated scaffolds that recapitulate the site-specific morphology of trabecular bone [23,25], ceramic scaffolds [1,2], and 3D-printed PCL scaffolds [4,8] support perfusion of hMSCs, but these scaffolds with tortuous pores are not amenable to imaging in the interior. Thus, the idealized geometry of cylindrical rods was selected in this study to enable fluorescence imaging of hMSC collection and comparison with theoretical models of collection efficiency [3,5,13]. While SLA has sufficient resolution for printing cylinders with trabecular thickness (Tb.Th.) comparable to human bone (190–198 μm) [22], the presence of residual cytotoxic monomers and photoinitiators renders the final parts unsuitable for cell culture [26]. Considering recent reports of injection-molded PS devices for single-cell imaging [10] and the use of SLA to fabricate molds with high deflection temperatures for injection molding PS [12], we used hybrid injection molding approach based on aluminum and SLA-printed molds to test multiple collector sizes and two array geometries. In thin-wall injection molding, the high melt viscosity of PS and small cross-sectional area of the feature create a significant pressure gradient along the length of the feature that limits its complete replication due to filling defects [27,28]. Wall thicknesses of 400 μm have been successfully molded for PS [28], while a 350-μm cavity exhibited differential shrinkage and warpage [29]. Thus, the smallest collector diameter was selected as 500 μm, since smaller sizes require more expensive and complex techniques such as micro-injection molding, rapid heat cycle molding (RHCM), and high-speed injection molding [28].
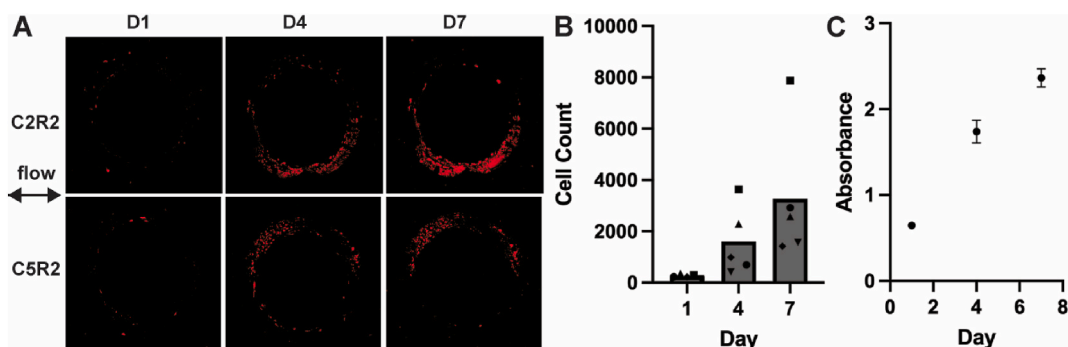
Fig. 7. Proliferation of hMSCs on the S_c-875 array. (A) Fluorescent images of z-stacks of CM-Dil⁺ hMSCs on days 1, 4, and 7 on collectors C2R2 and C2R5. (B) Cell counts on all 5 collectors calculated from the z-stacks and calibration curve. (C) MTS assay on days 1, 4, and 7.

Since only cells that follow grazing streamlines intercept the collectors in the low Stokes number flow field, multiple passes of the hMSC suspension through the array are required to collect a sufficient number of cells that can be expanded to confluence (Fig. 5D and E). Considering previous studies reporting 24 h perfusion times for hMSCs [1,2,4,8], cells were initially perfused through the array for 24 h at 56 mm s^{-1}, which generates a maximum shear stress of 1.4 Pa (Fig. 3). While shear stresses up to 2 Pa have been reported as optimal for cell attachment [30], these operating conditions resulted in extensive cell death, even at a reduced perfusion time of 6 h (Fig. 5A–C). Reduction of the superficial velocity to 33 mm s^{-1} (τ_{max} = 1.4 Pa) increased cell viability to 60–70 %, and further reduction of the velocity to 10 mm s^{-1} (τ_{max} = 0.2 Pa) increased the viability to 85–90 % (Fig. 5A–C). Perfusion of hMSCs through the array at 10 mm s^{-1} for 6 h resulted in a monotonic increase in collected cells over time (Fig. 5D and E), which were subsequently expanded for 7 days (Fig. 7). These findings are consistent with a previous study, which reported that a shear stress of 0.3 Pa applied for more than 6 h induced apoptosis of hMSCs [31]. Another study has reported that perfusion of hMSCs at 0.006 Pa for 24 h enhanced proliferation and osteogenesis [32]. However, the effects of shear stress on cell fate are time-dependent, with other studies finding that shear stresses up to 2.2 Pa stimulate chondrogenic and osteogenic differentiation for short periods of time [33,34]. Taken together, this study and others suggest that perfusion of hMSCs for 6 h at superficial velocities generating $\tau_{max} \leq 0.2$ Pa results in collection of cells at high viability.

Collection efficiencies calculated from interception theory, which neglects all external forces and assumes that cells following grazing streamlines intercept the collectors, were about two-fold higher than those calculated from the COMSOL simulations, which included gravitational and hydrodynamic forces (Fig. 6E and F). A previous study has reported that when the collector surface is perpendicular to the direction of flow, the effect of gravity on the cell deposition rate increases with decreasing flow rate [8]. In the present study, the calculated settling velocity of hMSCs is O(10^2) smaller than the superficial velocity (**Supplemental Information**) [5], and the collectors are parallel to the direction of flow. Considering that gravitational forces are minimal, the discrepancy between collection efficiencies calculated from interception theory and COMSOL simulations can be attributed in part to the repulsive hydrodynamic forces.

Experimental collection efficiencies measured by fluorescence microscopy were approximately 20 % lower than the simulated values, which suggests that electrostatic repulsion may also hinder cell collection. The hMSCs and PS collectors used in this study are negatively charged, resulting in a repulsive electrostatic force (**Supplemental Information**). As the hMSCs approach the collectors, they are pushed over the secondary energy barrier by attractive dispersion forces, resulting in capture by primary minimum [5]. Similar to hMSCs, bacteria are negatively charged colloidal particles that encounter electrostatic repulsion forces as they approach the negatively charged collectors [15]. For a suspension of bacteria transported through a packed bed of glass bead collectors, the collision efficiency was reduced by electrostatic repulsion in medium with ionic strength I = 1 M [35]. The present study was performed in lower ionic strength medium (0.147 M), resulting in a thicker electrical double layer. Thus, electrostatic repulsion likely reduced the collection efficiency of hMSCs compared with that predicted by Eq (5).

The experimental collected cell counts were more likely to follow a log-normal versus a normal distribution (Tables 2 and 3), which is consistent with previous studies reporting that a log-normal distribution accurately fit the experimental collision efficiency data for bacterial suspensions flowing through porous media [19,20]. The log-normal distribution is skewed for $0 < n_{cells} \leq \infty$, which represents a more realistic constraint on n_{cells} than the normal distribution (-$\infty \leq n_{cells} \leq \infty$) [19]. The simulated collected cell counts could not be fit to a log-normal distribution due to the fact that some cylinders collected zero cells. Simulating 10^6 cells in silico was cost-prohibitive with the computational power available. Thus, the relatively small sample size (5840 cells seeded) may have contributed to the variability in individual collector cell counts (52 < COV <90 %, Table 2). The variability in the experimental individual collector cell counts was higher for the constant N_c (105 % < COV <157 %) compared with the constant S_c (70 % < COV <84 %) arrays, which suggests that arrays with a constant distance between collectors yield more narrow collection efficiency distributions. Cells and collectors typically exhibit a distribution in physicochemical properties, including cell size, cell surface charge, and collector surface charge, which can result in a distribution of cell collection rates and efficiencies [15]. In a study investigating capture of bacteria in a porous medium, heterogeneity in the ζ-potential of bacteria resulted in a distribution of collection efficiencies when the suspension was filtered through a packed bed of glass beads [35]. Thus, heterogeneity in the surface charge of hMSCs could have contributed to the log-normal distribution of collected cell counts. However, the variability in cell counts can be reduced through longitudinal imaging of individual collectors.

After 7 days, the cell counts on the 5 imaged collectors ranged from 1750 to 8000 cells (Fig. 7B), corresponding to cell densities of 5.1 × 10^4 to 23.3 × 10^4 cells cm^{-2} for the 875-μm collectors. A recent study has reported that 80–100 % confluence is needed for osteogenic differentiation and that rat bone marrow MSCs are 100 % confluent at a cell density of 4.802 × 10^4 cells cm^{-2} [36]. These observations suggest that the hMSCs proliferated to near confluence on the collectors and may have formed multi-layers in some regions on C2R2 (Fig. 7A and B). When cultured in osteogenic medium, confluent hMSCs differentiate to osteoblasts, which deposit the osteoid extracellular matrix required for HSPC engraftment [1]. In ongoing studies, this rapid prototyping approach comprising CFD simulations and hybrid injection molding is being applied to optimize models of the endosteal niche that are amenable to longitudinal 3D imaging of the spatiotemporal dynamics of hematopoiesis.

6. Conclusions

A hybrid injection molding process was designed to fabricate perfusable PS collector arrays that mimic the 3D architecture of trabecular bone and are amenable to fluorescence microscopy. The rapid prototyping approach utilizing SLA-printed molds and injection molding allowed for high-throughput fabrication of collector arrays with variable geometries without the need for expensive and time-consuming tooling. Collectors were imaged over time to investigate the effects of array geometry on the collection efficiency

and proliferation of hMSCs. Experimental collection efficiencies agreed within a factor of 2 with those predicted by CFD simulations. For the constant collector spacing array design, the effect of collector diameter on collection efficiency followed a similar trend as that predicted by interception theory corrected for intermolecular attraction and hydrodynamic interactions. These findings highlight the utility of hybrid injection molding for rapid prototyping of collector arrays that model physiologically relevant bone marrow microenvironments and disease states without the need for tooling.

Funding

Data availability

Data will be made available upon request.

CRediT authorship contribution statement

Taylor E. Scott: Data curation, Formal analysis, Methodology, Software, Visualization, Writing – original draft, Writing – review & editing. **Tim Boccarossa:** Data curation, Methodology, Software. **David Florian:** Conceptualization, Investigation, Methodology. **Melissa A. Fischer:** Conceptualization, Funding acquisition, Writing – review & editing. **Sun H. Peck:** Formal analysis, Methodology, Resources, Writing – review & editing. **Michael R. Savona:** Conceptualization, Funding acquisition, Resources, Writing – review & editing. **Georg Pingen:** Conceptualization, Formal analysis, Methodology, Project administration, Resources, Software, Supervision, Writing – review & editing. **Scott A. Guelcher:** Conceptualization, Formal analysis, Funding acquisition, Methodology, Project administration, Supervision, Writing – original draft, Writing – review & editing.

Declaration of competing interest

The authors declare the following financial interests/personal relationships which may be considered as potential competing interests: Scott Guelcher reports financial support was provided by Incyte Corporation. Michael Savona reports financial support was provided by Incyte Corporation. Sun Peck reports financial support was provided by US Department of Veterans Affairs. If there are other authors, they declare that they have no known competing financial interests or personal relationships that could have appeared to influence the work reported in this paper.

Appendix A. Supplementary data

Supplementary data to this article can be found online at https://doi.org/10.1016/j.heliyon.2024.e35103.

References

[1] P.E. Bourgine, T. Klein, A.M. Paczulla, T. Shimizu, L. Kunz, K.D. Kokkaliaris, D.L. Coutu, C. Lengerke, R. Skoda, T. Schroeder, I. Martin, In vitro biomimetic engineering of a human hematopoietic niche with functional properties, Proc. Natl. Acad. Sci. U. S. A. 115 (2018) E5688–E5695, https://doi.org/10.1073/pnas.1805440115.

[2] A. Garcia-Garcia, T. Klein, G. Born, M. Hilpert, A. Scherberich, C. Lengerke, R.C. Skoda, P.E. Bourgine, I. Martin, Culturing patient-derived malignant hematopoietic stem cells in engineered and fully humanized 3D niches, Proc. Natl. Acad. Sci. U. S. A. 118 (2021), https://doi.org/10.1073/pnas.2114227118.

[3] W.B. Russel, D.A. Saville, W.R. Schowalter, Colloidal Dispersions, Cambridge University Press, 1989.

[4] A.C. Marin, T. Grossi, E. Bianchi, G. Dubini, D. Lacroix, micro-Particle tracking velocimetry and computational fluid dynamics study of cell seeding within a 3D porous scaffold, J. Mech. Behav. Biomed. Mater. 75 (2017) 463–469, https://doi.org/10.1016/j.jmbbm.2017.08.003.

[5] L. Spielman, Particle capture from low-speed laminar flows, Annu. Rev. Fluid Mech. 9 (1977) 297–319.

[6] S. Saini, T.M. Wick, Concentric cylinder bioreactor for production of tissue engineered cartilage: effect of seeding density and hydrodynamic loading on construct development, Biotechnol. Prog. 19 (2003) 510–521, https://doi.org/10.1021/bp0256519.

[7] D. Ali, Effect of scaffold architecture on cell seeding efficiency: a discrete phase model CFD analysis, Comput. Biol. Med. 109 (2019) 62–69, https://doi.org/10.1016/j.compbiomed.2019.04.025.

[8] A. Campos Marin, M. Brunelli, D. Lacroix, Flow perfusion rate modulates cell deposition onto scaffold substrate during cell seeding, Biomech. Model. Mechanobiol. 17 (2018) 675–687, https://doi.org/10.1007/s10237-017-0985-4.

[9] V.L. Mainardi, C. Arrigoni, E. Bianchi, G. Talo, M. Delcogliano, C. Candrian, G. Dubini, M. Levi, M. Moretti, Improving cell seeding efficiency through modification of fiber geometry in 3D printed scaffolds, Biofabrication 13 (2021), https://doi.org/10.1088/1758-5090/abe5b4.

[10] Y. Kim, J. Song, Y. Lee, S. Cho, S. Kim, S.R. Lee, S. Park, Y. Shin, N.L. Jeon, High-throughput injection molded microfluidic device for single-cell analysis of spatiotemporal dynamics, Lab Chip 21 (2021) 3150–3158, https://doi.org/10.1039/d0lc01245a.

[11] D. Dempsey, S. McDonald, D. Masato, C. Barry, Characterization of stereolithography printed soft tooling for micro injection molding, Micromachines 11 (2020), https://doi.org/10.3390/mi11090819.

[12] A. Palmer, J. Colton, Failure mechanisms in sterolithography injection molding tooling, Polym. Eng. Sci. 40 (2000) 1395–1404.

[13] L. Spielman, S. Goren, Capture of small particles by London forces from low-speed liquid flows, Environ. Sci. Technol. 4 (1970) 135–140.

[14] T. Hildebrand, P. Ruegsegger, Quantification of bone microarchitecture with the structure model Index, Comput. Methods Biomech. Biomed. Eng. 1 (1997) 15–23, https://doi.org/10.1080/01495739708936692.

[15] M. Elimelech, J. Gregory, X. Jia, R. Williams, Particle Deposition and Aggregation: Measurement, Modelling, and Simulation, vol. 117, Butterworth-Heinemann, 1995.

[16] M. Dominici, K. Le Blanc, I. Mueller, I. Slaper-Cortenbach, F. Marini, D. Krause, R. Deans, A. Keating, D. Prockop, E. Horwitz, Minimal criteria for defining multipotent mesenchymal stromal cells. The International Society for Cellular Therapy position statement, Cytotherapy 8 (2006) 315–317, doi: Q2183N8UT042W62H [pii]10.1080/14653240600855905.

[17] M. Rosen, Guidelines for part & tool design for molding rigid clear materials, Plast. Eng. 72 (6) (2016) 28–31, https://doi.org/10.1002/j.1941-9635.2016.tb01553.x.

[18] J. Fattori, Part 1: How to Properly Size Gates, Runners, and Sprues. Plastics Technology, 2020.

[19] D.G. Brown, A. Abramson, Collision efficiency distribution of a bacterial suspension flowing through porous media and implications for field-scale transport, Water Res. 40 (2006) 1591–1598, https://doi.org/10.1016/j.watres.2006.02.016.

[20] B.J. Mailloux, M.E. Fuller, T.C. Onstott, J. Hall, H. Dong, M.F. DeFlaun, S.H. Streger, R.K. Rothmel, M. Green, D.J.P. Swift, J. Radke, The role of physical, chemical, and microbial heterogeneity on the field-scale transport and attachment of bacteria, Water Resour. Res. 39 (2003), https://doi.org/10.1029/2002WR001591.

[21] W. Press, S. Teukolsky, W. Vetterling, B. Flannery, Numerical Recipes in C: the Art of Scientific Computing, second ed., Cambridge University Press, 1992.

[22] A. Alberich-Bayarri, L. Marti-Bonmati, R. Sanz-Requena, E. Belloch, D. Moratal, In Vivo trabecular bone morphologic and mechanical relationship using high-resolution 3-T MRI, Am. J. Roentgenol. 191 (2008) 721–726, https://doi.org/10.2214/AJR.07.3528.

[23] J.P. Vanderburgh, S.J. Fernando, A.R. Merkel, J.A. Sterling, S.A. Guelcher, Fabrication of trabecular bone-templated tissue-engineered constructs by 3D inkjet printing, Adv. Healthcare Mater. 6 (2017), https://doi.org/10.1002/adhm.201700369.

[24] M.L. Bouxsein, S.K. Boyd, B.A. Christiansen, R.E. Guldberg, K.J. Jepsen, R. Muller, Guidelines for assessment of bone microstructure in rodents using micro-computed tomography, J. Bone Miner. Res. 25 (2010) 1468–1486, https://doi.org/10.1002/jbmr.141.

[25] G.B. Lowen, J.P. Vanderburgh, D. Florian, T. Scott, J.A.R. Sterling, S.A. Guelcher, A perfusion bioreactor model of tumor-induced bone disease using human cells, Curr Protoc 2 (2022) e333, https://doi.org/10.1002/cpz1.333.

[26] B.J. O'Grady, M.D. Geuy, H. Kim, K.M. Balotin, E.R. Allchin, D.C. Florian, N.N. Bute, T.E. Scott, G.B. Lowen, C.M. Fricker, M.L. Fitzgerald, S.A. Guelcher, J. P. Wikswo, L.M. Bellan, E.S. Lippmann, Rapid prototyping of cell culture microdevices using parylene-coated 3D prints, Lab Chip 21 (2021) 4814–4822, https://doi.org/10.1039/d1lc00744k.

[27] G. Lucchetta, M. Sorgato, S. Carmignato, E. Savio, Investigating the technological limits of micro-injection molding in replicating high aspect ratio micro-structured surfaces, CIRP Annals 63 (2014) 521–524, https://doi.org/10.1016/j.cirp.2014.03.049.

[28] D. Masato, M. Sorgato, M. Babenko, B. Whiteside, G. Lucchetta, Thin-wall injection molding of polystyrene parts with coated and uncoated cavities, Mater. Des. 141 (2018) 286–295.

[29] D. Masato, J. Rathore, M. Sorgato, S. Carmignato, G. Lucchetta, Analysis of the shrinkage of injection-molded fiber-reinforced thin-wall parts, Mater. Des. 132 (2017) 496–504, https://doi.org/10.1016/j.matdes.2017.07.032.

[30] R. Cherry, Animal cells in turbulent fluids: details of the physical stimulus and the biological response, Biotechnol. Adv. 11 (1993) 279–299.

[31] D. Zhao, Y. Sun, X. Wei, H. Liang, L. Zhao, X. Dong, H. Chen, W. Chen, J. Yang, X. Wang, F. Gao, W. Yi, cIAP1 attenuates shear stress-induced hBMSC apoptosis for tissue-engineered blood vessels through the inhibition of the mitochondrial apoptosis pathway, Life Sci. 137 (2015) 81–88, https://doi.org/10.1016/j.lfs.2015.07.011.

[32] L. Jing, S. Fan, X. Yao, Y. Zhang, Effects of compound stimulation of fluid shear stress plus ultrasound on stem cell proliferation and osteogenesis, Regen Biomater 8 (2021) rbab066, https://doi.org/10.1093/rb/rbab066.

[33] A. Halim, A. Ariyanti, Q. Luo, G. Song, Recent progress in engineering mesenchymal stem cell differentiation, Stem Cell Rev Rep 16 (2020) 661–674, https://doi.org/10.1007/s12015-020-09979-4.

[34] G. Yourek, S. McCormick, J. Mao, G. Reilly, Shear stress induces osteogenic differentiation of human mesenchymal stem cells Regen Med 5 (2010) 713–724, https://doi.org/10.2217/rme.10.60.

[35] J.C. Baygents, J.R. Glynn, O. Albinger, B.K. Biesemeyer, K.L. Ogden, R.G. Arnold, Variation of surface charge density in monoclonal bacterial populations: implications for transport through porous media, Environ. Sci. Technol. 32 (1998) 1596–1603, https://doi.org/10.1021/es9707116.

[36] F.A.M. Abo-Aziza, A.Z. A, The impact of confluence on bone marrow mesenchymal stem (BMMSC) proliferation and osteogenic differentiation, Int. J. Hematol. Oncol. Stem Cell Res. 11 (2017) 121–132.